# Characterization and Structural Analysis of an Active Particulate Methane Monooxygenase Trimer from *Methylococcus capsulatus* (Bath)†

Ashraf Kitmitto,*,‡,§ Natalia Myronova,§,|| Piku Basu,|| and Howard Dalton||

*School of Medicine, University of Manchester, Manchester M60 1QD, U.K., and Department of Biological Sciences, University of Warwick, Coventry CV4 7AL, U.K.*

*Received May 4, 2005; Revised Manuscript Received June 15, 2005*

ABSTRACT: The oxidation of methane to methanol in methanotrophs is catalyzed by the enzyme methane monooxygenase (MMO). Two distinct forms of this enzyme exist, a soluble cytoplasmic MMO (sMMO) and a membrane-bound particulate form (pMMO). We describe here the biochemical characterization of a stable and active purified pMMO hydroxylase (pMMO-H) and report a three-dimensional (3D) structure, determined by electron microscopy and single-particle analysis at 23 Å resolution. Both biochemical and structural data indicate that pMMO hydroxylase is trimeric, with each monomer unit comprised of three polypeptides of 47, 26, and 23 kDa. Comparison of the recent crystal structure [Lieberman, R. L., and Rosenzweig, A. C. (2005) *Nature 434*, 177] of an uncharacterized pMMO-H complex with the three-dimensional (3D) structure determined here yielded a good match between the principal features and the organization of the enzyme monomers into trimers. The data presented here advance our current understanding of particulate methane monooxygenase function by the characterization of an active form of the enzyme and the corresponding 3D structure.

Methane monooxygenases (MMOs)[1] catalyze the oxygenation of methane to methanol and are essential components of the methane oxidation pathway in methanotrophs. Methanotrophic bacteria are capable of converting methane to carbon dioxide and therefore serve as an important methane sink (*1*) with a potential role for combating global warming (*2*). Methane monooxygenases also possess the unique ability to oxidize a broad range of hydrocarbons in addition to methane (*3*), and as such, they have a varied role in biological and ecological systems (*4*−*7*).

There are two different forms of MMO that are expressed in response to the copper-to-biomass ratio (*8*). At low concentrations of copper, the soluble form of the enzyme (sMMO) is presented in a small subset of bacteria, while with a high copper content (>0.2 mg/L), networks of the intracytoplasmic membrane are developed and MMO is expressed as a membrane-associated form of the enzyme (pMMO). sMMO has been extensively studied and is well-characterized, with the X-ray crystal structure of the sMMO hydroxylase [isolated from *Methylococcus capsulatus* (Bath)] being reported more than 12 years ago (*9*, *10*). However, the presence of the soluble MMO is restricted to a limited number of methanotrophic strains (*11*). Many environments are able to sustain sufficient levels of copper for expression of functional pMMO, and as such, pMMO is present in virtually all known methanotrophs (*12*, *13*). However, due to a number of factors such as instability upon removal from the membrane, this form of the enzyme is less well characterized in comparison with sMMO in terms of both its quaternary organization and its mechanism of methane oxidation.

In accordance with published results for pMMO purified from *M. capsulatus* (Bath) (*14*−*17*) and *Methylosinus trichosporium* OB3b (*18*, *19*), it is generally accepted that the enzyme consists of at least the hydroxylase (which we call pMMO-H in this paper) formed by three polypeptides with molecular masses of approximately 47 kDa ($\beta$, pmoB subunit), 26 kDa ($\alpha$, pmoA subunit), and 23 kDa ($\gamma$, pmoC subunit), encoded by the *pmoA*, *pmoB*, and *pmoC* genes, respectively (*20*). Radiolabeling experiments with the suicide substrate acetylene have suggested that the active site is localized to the $\alpha$ subunit and may also involve the $\beta$ subunit (*21*, *22*). Recently, a structural model based on gene sequence analysis of the 26 kDa subunit of the hydroxylase from *M. capsulatus* (Bath) proposed that it comprised seven transmembrane helices (*23*). It was suggested that four of these helices and one loop region participated in the formation of the active center and that substrate access occurred only from the periplasmic side of the enzyme. Any sensible structural model of hydroxylase components will require knowledge of its subunit arrangement. To that effect, several studies have attempted to determine subunit stoichiometry by gel

† This work was funded through grants to H.D. from the Biotechnology and Biological Sciences Research Council (B13749 and C00194X) and INTAS 03-51-3945.

* To whom correspondence should be addressed. E-mail: ashraf.kitmitto@manchester.ac.uk. Telephone: +44 (0) 161 2004186. Fax: +44 (0) 161 2360409.

‡ University of Manchester.

§ These authors contributed equally to this report.

|| University of Warwick.

[1] Abbreviations: MMO, methane monooxygenase; pMMO, particulate methane monooxygenase; MDH, methanol dehydrogenase; ICM, intracytoplasmic membrane; DDM, dodecyl $\beta$-D-maltoside; PIPES, 1,4-piperazine bis(ethanesulfonic acid, sodium salt); BN-PAGE, blue native polyacrylamide gel electrophoresis; SDS−PAGE, sodium dodecyl sulfate−polyacrylamide gel electrophoresis; SPA, single-particle analysis.

10.1021/bi050820u CCC: $30.25 
Published on Web 07/26/2005

filtration and PAGE techniques. An overall mass of 326 kDa was reported for *M. trichosporium* OB3b pMMO preparations comprising two subunits with molecular masses of 25 and 41 kDa and a trace of the 26 kDa component (*18*) with no indication of oligomeric structure. The hydroxylase from *M. capsulatus* (Bath) was estimated to have an overall mass of 200 kDa by BN-PAGE with a proposed dimeric $\alpha_2\beta_2\gamma_2$ arrangement (*16*). These authors also observed a 440 kDa band which they suggested was the tetramer, although a similar value of 220 kDa was reported by Chan and co-workers (*24*), and these gel filtration data were interpreted as a monomeric structure of pMMO surrounded by 240 detergent molecules. It is clear from these reports that some ambiguity exists in establishing the structure of the quaternary organization of the fully functional protein. In this study, we have used a combination of PAGE with MALDI mass spectrometric analysis and sedimentation equilibrium to estimate the molecular mass of the holoenzyme.

In addition to the instability of the pMMO complex *in vitro*, structural analyses of membrane proteins are generally less well developed than for soluble proteins due, for example, to difficulties in overexpression and purification and the requirement for detergents and lipids for stability. A significant step forward toward understanding the quaternary organization of pMMO-H has been the recent publication of a crystal structure of the purified enzyme (2.8 Å resolution) (*25*). pMMO-H was shown to be trimeric, ~105 Å in height, and 90 Å in diameter, roughly resembling a cylinder. However, no assessment of the activity of the crystals or biochemical analysis of the oligomeric form was undertaken, and it is quite probable, from their description of the enzyme preparation, that the crystals were inactive. We have independently, and in parallel, characterized the oligomeric form and structure of an active form of pMMO-H. Using electron microscopy coupled with single-particle analysis (SPA), we have also determined the three-dimensional (3D) structure of pMMO-H and shown it to be trimeric. Over the past 10 years, SPA has proven to be extremely successfully used in studying the quaternary organization of multimeric polytopic proteins at medium resolutions (*26*−*28*) that are not readily amenable to techniques such as X-ray crystallography and NMR. SPA has been proven to be suitable for relatively small proteins (*29*, *30*) as well as large macromolecular complexes such as the ribosome (for a review, see ref *31*). We report here the 3D structure of a highly active form of the pMMO-H enzyme at a final resolution of 23 Å. We have identified side "holes" in the periplasmically exposed region of the protein. These areas are not initially apparent from the crystal structure, although a more detailed comparison of the two independent structures indicates their presence. We propose that these areas show potential as the substrate entry site.

## EXPERIMENTAL PROCEDURES

### *Cultivation of M. capsulatus (Bath)*

All experiments described here employ the *M. capsulatus* (Bath) from the University of Warwick culture collection. Methanotrophs were grown in nitrate minimal salts medium (*32*). A final $CuSO_4$ concentration of 40 $\mu$M was used in medium when pMMO-expressing cells were grown. Large-scale fermentation of *M. capsulatus* (Bath) was performed in a 100 L fermenter as described in ref *14*. Cells were harvested and washed with 25 mM PIPES (pH 7.2) and resuspended in the same buffer. Concentrated cells were frozen and stored at −80 °C.

### *Membrane Isolation, Solubilization, and Purification of pMMO*

Thawed cells were washed with 25 mM PIPES (pH 7.2), centrifuged at 12000*g* for 15 min at 4 °C, and resuspended in the same buffer supplemented with DNase I (a few crystals), 1 mM benzamidine, 40 $\mu$M $CuSO_4$, and 1% (w/v) CHAPS (final concentration). The cells were broken as follows. Suspended cells were passed through a Constant Cell Disrupter (Constant Systems, Warwick, U.K.) three times at 25 MPa and 4 °C. Unbroken cells and debris were removed by centrifugation at 12000*g* for 25 min at 4 °C. The supernatant was centrifuged at 144000*g* for 90 min, and the pellet was resuspended in the 25 mM PIPES (pH 7.2) containing 0.5 M NaCl and 1 mM benzamidine. This process was repeated at least twice to remove soluble proteins. Finally, the pellet containing membrane-embedded pMMO ($pMMO^m$) was resuspended in the same buffer at a protein concentration of 25−30 mg/mL. Solubilization of $pMMO^m$ and purification using gel-filtration chromatography were performed as described in ref *14*. Further purification of pMMO was carried out on the anion-exchange MonoQ-10 column. Concentrated fractions after the Superdex S200 column, mainly containing pMMO-H (hydroxylase) with a small trace of the methanol dehydrogenase (MDH), were applied to anion-exchange MonoQ-10 column which was equilibrated in precooled (4 °C) 25 mM PIPES (pH 7.2) supplemented with 0.01% (w/v) dodecyl $\beta$-D-maltoside and 1 mM benzamidine. An increasing (0−1 M) NaCl gradient was used to elute the pure pMMO hydroxylase, which was concentrated using an Amicon stirred cell with a PM10 ultrafiltration membrane.

### *Protein Concentration*

Protein concentrations were determined according to a modified Lowry protocol (*33*) with BSA as the standard.

### *Gel Electrophoresis*

BN-PAGE was carried out with a 4−17% polyacrylamide gradient gel, prepared by the method of Schägger and von Jagow (*34*, *35*). Samples (50−100 $\mu$g of protein per lane) were mixed with 0.5 M aminocaprionic acid and loaded on the top of a 4% stacking gel. The gel was run at 8 °C at a 15 mA constant current and 70−120 V. When the samples had completely passed through the stacking gel, the voltage was gradually increased to 300 V. The running time was ~6 h. The cathode buffer [50 mM Tricine and 7.5 mM imidazole (pH 7.0)] first contained 0.02% Coomassie blue dye G-250. It was replaced with a buffer containing 0.002% Coomassie blue dye G-250 after one-third of the run. After electrophoresis, gels were further destained in 25% methanol and 10% acetic acid. To determine the molecular mass of pMMO-H, several standard proteins with known molecular masses were used: thyroglobulin (669 kDa), ferritin (440 kDa), catalase (232 kDa), lactate dehydrogenase (140 kDa), and albumin (bovine serum) (66 kDa).

SDS−PAGE (12%) was performed according to the method of Laemmli (*36*) at room temperature and 200 V. Protein bands on the SDS−PAGE gels were visualized with Coomassie blue R-250 (0.1%, w/v) in 10% (v/v) methanol and 10% (v/v) glacial acetic acid. The gel was then destained by incubation in a solution of methanol, glacial acetic acid, and water (4:1:5, v/v). The SDS−PAGE gels were calibrated using Dalton Mark VII-L markers (Sigma).

### *Enzyme Activity Assay*

The activity of pMMO at each stage of membrane isolation and purification was assayed by following oxidation of propylene to propylene oxide using a Pye Unicam model GCV gas chromatograph (Pye Unicam, Cambridge, U.K.) fitted with Porapak Q column. The samples (5 mg/mL) were placed in a 2 mL vial and sealed, and 1 mL of air was replaced with 1 mL of propylene. To give optimal activity, the reaction mixtures were supplemented with an appropriate addition of copper sulfate (50−20 $\mu$M). After incubation for 1 min, 5 mM NADH (natural electron donor) was added to membrane-embedded pMMO sample. For solubilized and purified pMMO, the assay was carried out with 10 mM duroquinol (artificial electron donor) dried on the bottom of the vial. The final volume of the assayed sample was always 100 $\mu$L. The samples were incubated at 45 °C in a shaking water bath. After incubation for 3 min, a 5 $\mu$L liquid sample was injected into the gas chromatograph, calibrated with 2 mM propylene oxide (PO).

### *Analytical Gel Filtration*

Calibration of preparative grade Superdex S200 (Amersham Pharmacia Biotech) (1.5 cm × 98 cm) for molecular mass estimation was carried out by equilibrating the column with 10 mM PIPES (pH 7.2) containing 0.01% (w/v) *n*-dodecyl $\beta$-D-maltoside at a flow rate of 2 mL/min. The molecular mass determination of pMMO was made by comparing the $V_e/V_o$ ratio of pMMO with the $V_e/V_o$ ratio of four proteins with known molecular masses [Bio-Rad calibration kit, aldolase (158 kDa), catalase (232 kDa), ferritin (440 kDa), and thyroglobulin (669 kDa)], where $V_e$ is the elution volume and $V_o$ is the void volume of the column, which was taken as the elution volume required for the elution of blue dextran (2000 kDa) from the column. The calibration curve was prepared by plotting the logarithms of the known molecular masses of protein standards against their $V_e/V_o$ values. The corresponding molecular masses could then be deduced from the calibration curve by using the experimentally determined $V_e/V_o$ value of pMMO.

### *Analytical Ultracentrifugation*

Sedimentation−equilibrium experiments were performed in a Beckman Optima XL-A analytical ultracentrifuge at 4 °C. The pMMO hydroxylase was analyzed at a concentration 5 mg/mL in 20 mM PIPES (pH 7.2). Buffers containing $D_2O$:$H_2O$ ratios between 0 and 50% were prepared; the protein was added to the appropriate buffer, and samples were concentrated to give a final volume of 200 $\mu$L. Buffer and detergent densities were measured at 4 °C using a Precision density meter (model 02C, Anton Paar, Graz, Austria). Samples and their appropriate buffers were loaded into their respective channels in 12 mm multichannel cells. Equilibrium runs were carried out at rotor speeds of 10 000, 12 000, and 15 000 rpm until equilibrium was achieved at each speed. Samples were prespeeded at 45 000 rpm to obtain the baseline absorbance for each sample. Scanning absorbance optics were used at wavelengths of 280 nm. Data from one speed only (10 000 rpm) were used for analysis as this proved to be the best condition. Molecular masses for the protein at each $D_2O$:$H_2O$ ratio were obtained using the manufacturer's software package (Beckman Instruments, Inc., Fullerton, CA). The contribution of detergent to the molecular mass of pMMO-H was calculated according to the method of Kleinekofort et al. (*37*).

### *Mass Spectrometric Analysis of pMMO-H*

Protein bands from BN-PAGE gels were excised, destained, reduced, alkylated, and digested with trypsin, and the resulting peptides were extracted using the Micromass Mass Prep Station running the standard digestion protocol supplied by the manufacturer. The tryptic peptides were transferred to a cooled second 96-well microtiter plate and, if necessary, stored at −80 °C. A 2 $\mu$L aliquot of the tryptic extract was mixed with 2.0 $\mu$L of a 50% acetonitrile, 0.05% trifluoroacetic acid, 49.5% water solution containing 4 mg/mL $\alpha$-cyano-4-hydroxycinnamic acid (matrix), and 1 $\mu$L was spotted onto the MALDI target plate. The lock mass wells on the target plate were spotted with 1 $\mu$L of a 0.2 $\mu$M solution of four peptides [human adrenocorticotropic hormone (ACTH), rennin, GLU fibrinopeptide B, and angiotensin I] as a standard. The tryptic peptides were analyzed using reflectron mode on a Waters MS Technologies MALDI micro MX mass spectrometer controlled by Mass Lynx 4.0 software, fitted with a nitrogen UV laser (337 nm) incorporating a time-of-flight (TOF) mass analyzer. Data were collected over the mass/charge (*m*/*z*) range of 1000−3000, and mass drift was corrected against the $[M + H]^+$ ion of ACTH occurring at *m*/*z* 2465.199. The data were processed using the Micromass Global Server 2.1 search engine. Search parameters specify up to one missed cleavage site, a 100 ppm tolerance against the database-generated theoretical masses, and a minimum of one matched peptide with a list of the 20 highest-scoring entries produced. Each suggested protein identification was confirmed or rejected by a comparison of the theoretical and observed data.

### *Electron Microscopy*

*Membrane-Embedded pMMO.* Intracytoplasmic membranes ($pMMO^m$) extracted from whole cells were resuspended in 25 mM PIPES buffer (pH 7.25) containing 1 mM benzamidine and 100 mM NaCl. Membranes were also washed with 25 mM PIPES buffer (pH 7.25), 10 mM EDTA, and 1 M NaCl and then diluted for a protein concentration suitable for EM studies (e.g., ∼100 $\mu$g/mL). Samples were mounted onto carbon-coated 400 mesh copper grids after glow discharging, and excess protein was blotted with filter paper (Whatman 50), washed twice with detergent-free buffer [25 mM PIPES (pH 7.25) and 100 mM NaCl], negatively stained using 4% (w/v) uranyl acetate as described in ref *38*, and examined in a Tecnai 10 transmission electron microscope operated at an accelerating voltage of 100 kV. Electron micrographs were recorded at a calibrated magnification of 44500× on Kodak Electron Image film SO-163.

Electron micrographs were digitized (UMAX PowerLook 3000 Scanner) at a scan step of 16 $\mu$m (3.6 Å/pixel at the specimen level).

*Electron Crystallography.* Crystalline areas were treated separately; the contrast transfer function (CTF) was corrected using the CRISP Image processing software suite (*39*) and subjected to three rounds of lattice unbending to correct for lattice distortions using programs within the Medical Research Council crystallographic software (*40*). Average cell dimensions, p1, for the two-dimensional (2D) arrays ($n = 4$) were as follows: $a = 116.0 \pm 9.2$ Å, $b = 113.6 \pm 9.7$ Å, and $\gamma = 122.9 \pm 2.5°$. Using the CRISP software, a range of plane groups were tested for each crystal with *p*3, *p*312, and *p*321 giving the lowest phase residuals, 8.5, 21.3, and 12.5°, respectively.

*Purified pMMO Hydroxylase (pMMO-H).* pMMO-H was resuspended in 25 mM PIPES buffer (pH 7.25) containing 100 mM NaCl and 0.01% (w/v) *n*-dodecyl $\beta$-D-maltoside for a concentration of ~100 $\mu$g/mL as described above. Micrographs were recorded under low-dose conditions.

*3D Image Processing of pMMO-H.* The 3D structures of pMMO-H were generated using the common line projection matching methods employed in EMAN (*41*). No correction for the contrast transfer function was made since the micrographs used had the first minimum of the power spectrum in the range of 15−20 Å; 2482 pMMO-H complexes were selected interactively using the graphical interface boxer (EMAN processing software) from digitized micrographs (3.6 Å/pixel at the specimen level) into a box of 56 × 56 pixels. A preliminary 3D model was calculated from a set of reference-free class averages that represented distinct views of the complex, generated after band-pass filtering and centering of the particles. The preliminary 3D model was iteratively refined using a projection matching routine, whereby projections with uniformly distributed orientations of the preliminary 3D model were used as references for classification of the raw data set, with the class averages from this step used to construct a new 3D model. Convergence, i.e., stabilization of the 3D structure, was monitored by examining the Fourier shell correlation (FSC) of the 3D models generated from each iteration. Volumes were separately calculated with either *C*1, *C*2, or *C*3 symmetry applied. For the *C*1 and *C*2 volumes, the class averages used to generate the preliminary model were selected by the user. In each reconstruction, the final 3D volume was derived from eight rounds of iterative refinement. To test the robustness of the final volumes, several different starting models were employed; all produced a similar convergence. In addition, to further examine the effects of employing a different start model upon the reconstructions in *C*1 and *C*3, the crystal structure of a trimeric pMMO-H (*25*) (PDB entry 1YEW) after a Gaussian low pass filter to 15 Å had been applied was used as the start model (threed.0a.mrc). The resulting structures were consistent with those presented in this report.

The resolution of each reconstruction was assessed following established procedures (*42*, *43*). In brief, the data set was divided into two, with volumes calculated for the two subsets, and the resolution estimated by the Fourier shell correlation coefficient (FSC) with the resolution limit taken to be where the FSC value fell below 0.5.

*Symmetry Analysis of pMMO-H*

Two different methods of analysis were employed for symmetry analysis. Rotational symmetry analysis of the individual pMMO-H particles was initially performed in EMAN using "startcsym". The startcsym command searches the raw images for particles with *n*-fold rotational symmetry, corresponding to the "top" view, with "side views" having good mirror symmetry but poor *n*-fold rotational symmetry. Class averages are then generated for each of these two views. The unsymmetrized top view can then be compared with the symmetrized view. A range of possible symmetries (*C*2−*C*8) was tested. In a different approach, SPIDER programs (*44*) were implemented to examine the symmetry of the final *C*1 3D volume by a rotational self-orientation search. A back projection of the *C*1 volume in Figure 4A projected along the longitudinal axis of rotational symmetry was generated to determine the rotational symmetry (using the SPIDER command OR 2M).

## RESULTS

*Electron Micrographs of Intracytoplasmic Membrane Preparations*

Intracytoplasmic membranes (ICMs) from *M. capsulatus* (Bath) were isolated as described previously (*14*) with an average specific activity of 230 nmol of propylene oxide per minute per milligram of protein using 5 mM NADH as a reductant. Presented in Figure 1A is an electron micrograph of negatively stained ICMs, prepared as described in Experimental Procedures, after washing with 10 mM EDTA and 1 M NaCl. The micrograph shows a large membrane sheet containing closely packed white stain-excluding protein complexes characterized by a central stain cavity (examples indicated by black arrowheads). Close examination of the ICMs found several small areas where the membrane-embedded complexes had formed partially ordered two-dimensional (2D) crystals; an example of such an area is highlighted in the figure with dashed lines. The Fourier transform of the crystalline area after three rounds of lattice unbending to correct for lattice distortions, using the Medical Research Council crystallographic program suite (*40*), is shown in panel B. Refinement of the lattice found the lowest phase residual for a *p*3 symmetry suggesting a trimeric organization, with the corresponding projection map in Figure 1C. The projection map shows a complex approximately 90 Å across (edge to edge) with three protein densities surrounding a central cavity approximately 25 Å in diameter.

Prior to the ICMs being washed with EDTA and NaCl, extensive aggregation of the membranes was observed. Subsequent washing resulted in well-separated membranes, though some association was still observed as indicated by the black arrow Figure 1A. SDS−PAGE (Figure 1D) of washed ICMs showed the presence of protein bands with molecular masses corresponding to those associated with pMMO, i.e., 47, 26, and 23 kDa. Several other less abundant polypeptides, e.g., 37 and 35/32 kDa, a doublet at 21/23 kDa, 16 kDa, and 7 and 6 kDa, were also detected. The polypeptides giving rise to these bands were found to be more abundant in the sample prior to washing, suggesting that they are not embedded in the lipid bilayer and may be proteins loosely associated with the pMMO complex (data

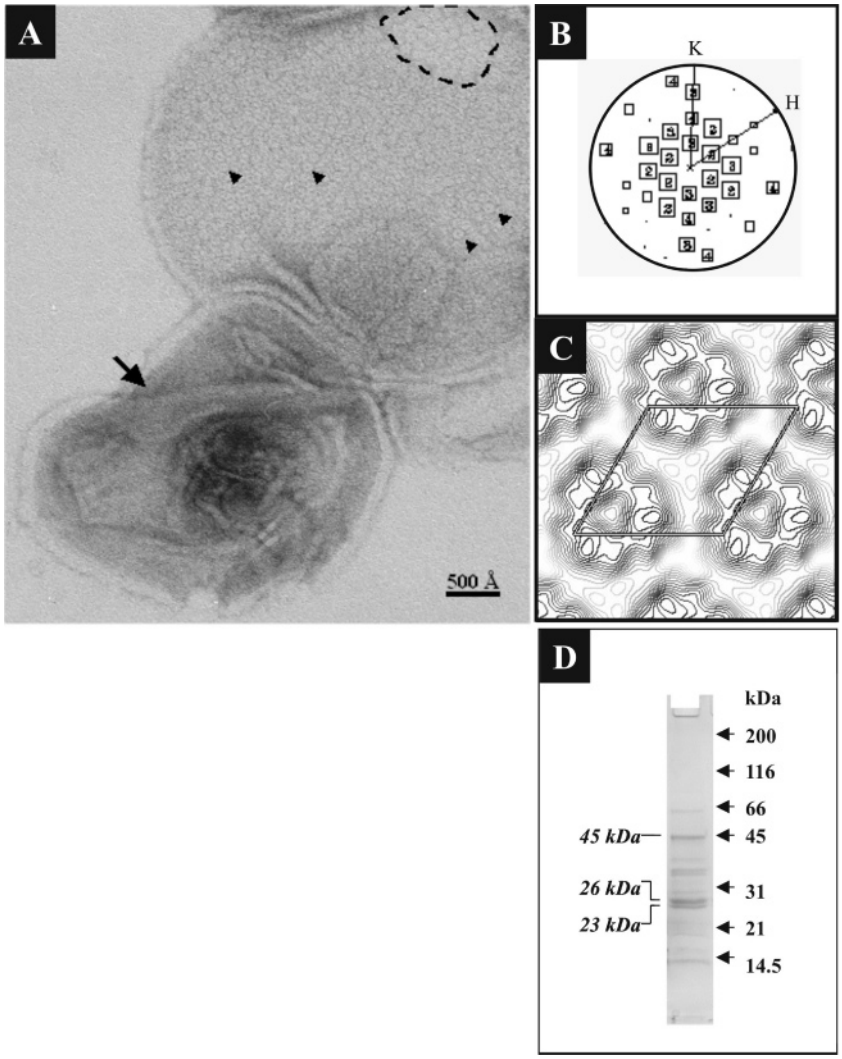


FIGURE 1: Characterization of membrane-embedded pMMO complexes. (A) Electron micrograph of negatively stained intracytoplasmic membranes (ICMs) isolated from *M. capsulatus* (Bath) after washing with 25 mM PIPES buffer (pH 7.25), 10 mM EDTA, and 1 M NaCl. Protein is visualized as white stain, excluding densities with examples indicated by black arrowheads. The large black arrow indicates associated membrane sheets. (B) Plot of the signal:noise ratios of peaks in the Fourier transform of the crystalline area enclosed by the dashed lines in panel A after lattice correction. The larger boxes and lower number correspond to a greater signal:noise ratio. (C) *p*3 projection map of the crystalline area. Unit cell dimensions (indicated by parallelogram) are as follows: $a = b = 107$ Å and $\gamma = 120°$. (D) SDS−PAGE (12%) of EDTA/salt-washed membrane-embedded particulate methane monooxygenase from *M. capsulatus* (Bath) with protein bands visualized by Coomassie brilliant blue R-250 staining.

not shown). Previous work by Zahn and DiSpirito (*45*) had assigned the 37 and 21 kDa proteins as cytochromes $b_{559}$ and $b_{569}$, respectively, with the 35/32 kDa protein suggested by Nguyen and co-workers (*17*) being a product of proteolysis of the 47 kDa subunit of pMMO. There was also a relatively weak band at ~63 kDa that was observed to be significantly reduced in intensity after salt washing. This band was identified by means of tryptic digestion and MALDI peptide mass fingerprinting as large subunits of methanol dehydrogenase (MDH) from *M. capsulatus* (Bath) with 66% sequence coverage.

Table 1: Specific Activity of pMMO at Various Stages of Membrane Isolation and Purification

| sample | specific activity (nmol of PO produced $min^{-1}$ $mg^{-1}$) 5 mM NADH (natural reductant) | 10 mM duroquinol (artificial reductant) |
|---|---|---|
| membrane-bound | 230 | 114 |
| solubilized | no activity | 96 |
| partially purified pMMO + MDH[a] | no activity | 64 |
| purified | no activity | 34 |

[a] The SDS−PAGE gel of partially purified pMMO and MDH has been published in Figure 1 of ref *14*.

*Purification of pMMO-H*

The specific activities of pMMO at the various stages of isolation and purification are presented in Table 1. The specific activity of our purified pMMO was 34 nmol of propylene oxide per minute per milligram of protein with 10 mM duroquinol as an artificial reductant (*46*), a value that is still higher than most of the published results (*47*). Purified pMMO was shown to be composed of three proteins with molecular masses of 47, 26, and 23 kDa, therefore corresponding to pMMO hydroxylase (pMMO-H) as shown in Figure 2 (inset, top left corner). A feint band at ~32 kDa was also discernible. Figure 2 presents an electron micrograph of the purified pMMO-H after negative staining as

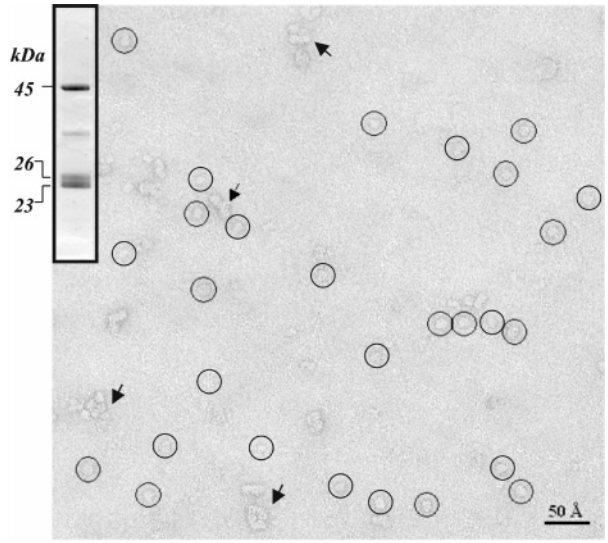


FIGURE 2: Characterization of purified pMMO hydroxylase (pMMO-H). A field of negatively stained purified pMMO-H illustrating a homogeneous population of protein complexes. Examples of pMMO-H complexes are ringed by black circles. The black arrows indicate areas of protein aggregation, though from the sample micrograph it is clear that well-defined single complexes suitable for SPA predominate. The inset is a 12% SDS−PAGE gel of the purified pMMO-H, stained with Coomassie brilliant blue R-250.

described in Experimental Procedures showing a homogeneous field of protein complexes (examples ringed by black circles). Some aggregation of the sample was also apparent (indicated by black arrows in Figure 2) under the negative staining conditions; however, well-defined single complexes were abundant with a final data set comprised of ~2500 particles.

*Molecular Mass Estimation of pMMO-H*

We applied several different approaches for the determination of the molecular mass of pMMO-H.

*Analytical Gel Filtration.* Presented in Figure 3A is a calibration curve of a Superdex S200 (Pharmacia) size-exclusion column determined by eluting four proteins with known molecular masses. When this method was applied, the molecular mass of purified pMMO was estimated to be 390 kDa. The molecular mass is close to that of ~326 kDa for purified pMMO from *M. trichosporium* OB3b (*18*). This technique gives an approximate molecular mass value, which included the mass of the protein and mass of the bound detergent (*48*).

*Sedimentation Equilibrium.* For a more accurate determination of the molecular mass of pMMO-H that takes into consideration any bound detergent, we employed sedimentation equilibrium analysis. The molecular mass ($M$) is the molecular mass of the pure protein, excluding bound detergent and other solvent compounds, and is related to the experimentally determined protein concentration ($c$) as a function of the radial position ($r$) by the relation

$$(2RT/\omega^2)(\ln c/r^2) = M(1 - \varphi'\rho)$$

where $R$ is the gas constant, $T$ is the absolute temperature, $\omega$ is the angular velocity, $\rho$ is the density of the solvent, and $\varphi'$ is the effective partial specific volume, which includes the true partial specific volume and the effects of integration with detergent (DDM). Since the partial specific volume of the pMMO−DDM complex is unknown, the molar mass of the protein moiety cannot directly be derived from the effective molar mass of the complex [$M_b = M_{pMMO-DDM}(1 - \varphi'_{pMMO-DDM}\rho) = M_{pMMO-H}(1 - \varphi'_{pMMO-H}\rho) + M_{DDM}(1 - \varphi'_{DDM}\rho)$]. However, via determination of the $M_b$ as a function of solvent densities by varying the ratio of $H_2O$ and $D_2O$, the molar mass of the protein moiety can be evaluated by extrapolation to the density of dodecyl maltoside (DDM) (*37*).

Following the procedure as described in ref *37*, this method gave a calculated molecular mass for pMMO-H of 313 ± 25 kDa.

*Electrophoresis.* Blue native gel electrophoresis (BN-PAGE) established by Schägger (*35*) was also used to determine the molecular mass and oligomeric state of membrane proteins. Analysis of purified pMMO-H using BN-PAGE resulted in a single band (Figure 3B, lane 1) with an estimated mass of 380−410 kDa. To be sure that the observed protein band consisted of pMMO-H only, the band was excised from the gel, soaked in a solution of 10% SDS and $\beta$-mercaptoethanol for 2 h, and subjected to SDS−PAGE. The size and composition of subunits of the protein corresponded to those of pMMO-H (data not shown). Furthermore, the excised protein band (Figure 3B, lane 1) was characterized by tryptic digestion and MALDI peptide mass fingerprinting and identified as the pmoB subunit of particulate methane monooxygenase with 45% sequence coverage. The presence of pmoA and pmoC was confirmed by limited (6 and 3.7%, respectively) sequence coverage of digested peptides.

*3D Structure of pMMO-H and Symmetry Analysis*

Eight rounds of angular refinement were applied to 2500 pMMO-H protein complexes to determine the final three-dimensional structure without imposing any symmetry constraints, i.e., *C*1, implementing established procedures in the EMAN image processing software suite (*41*). The surface-rendered volume (displayed at $2\sigma$ above the mean density) in Figure 4A shows a view of the complex with three defined protein densities (labeled 1−3) surrounding a central cleft or canyon ~25−30 Å in diameter. Figure 4B displays a putative side view (i.e., perpendicular to the membrane normal) of the complex, illustrating that pMMO-H is roughly shaped like a truncated cone, being wider at one end termed the "base", ~135 Å in diameter, and tapering upward toward three protein densities forming a domain we have called the "neck", ~95 Å across. Overall, the pMMO-H complex is ~125 Å tall. The complex is characterized by a central cavity that penetrates the complex by ~60 Å. The resolution of the reconstructed *C*1 volume was determined to be ~30 Å (data not shown).

To further examine the oligomeric form of the purified pMMO-H, we also tested the symmetry of the *C*1 complex using two different methods: (i) applying startcsym in EMAN (*41*) and (ii) a self-orientation search using SPIDER (*44*). The startcsym command searches the raw images for particles with *n*-fold rotational symmetry, corresponding to the top view, with side views having good mirror symmetry but poor *n*-fold rotational symmetry. A range of possible symmetries (*C*2−*C*8) was tested (data not shown), finding

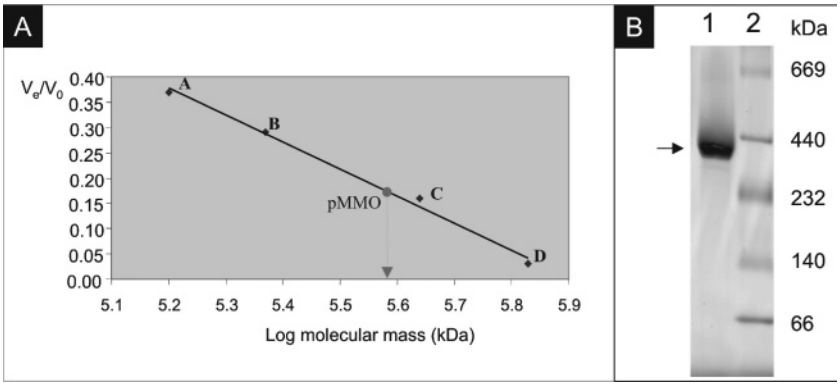


FIGURE 3: Molecular mass estimation of pMMO-H. (A) Gel filtration chromatography S200 (Pharmacia) size-exclusion column. Molecular mass standards used to calibrate the column are (A) aldolase (158 kDa), (B) catalase (232 kDa), (C) ferritin (440 kDa), and (D) thyroglobulin (669 kDa). The approximate molecular mass of the detergent-bounded pMMO-H was estimated to be 390 kDa. (B) Blue native PAGE (BN-PAGE), with a 4 to 17% gradient of pMMO−H. In lane 1, BN-PAGE with 0.5 M 6-aminocaprionic acid in sample buffer reveals the pMMO-H band at ~380−410 kDa (pMMO-H, confirmed by MS). In lane 2 are molecular mass standards: thyroglobulin (669 kDa), ferritin (440 kDa), catalase (232 kDa), lactate dehydrogenase (140 kDa), and albumin (bovine serum) (66 kDa).

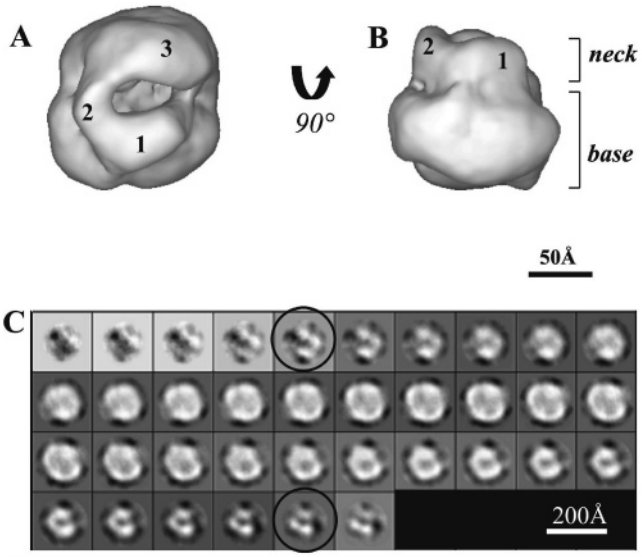


FIGURE 4: 3D structure of purified pMMO-H refined in *C*1. (A) Putative periplasmic face of the complex characterized by three protein densities (labeled 1−3) surrounding a central cleft. Surface rendered (2$\sigma$ above the mean density calculated to encompass a protein mass of ~300 kDa). (B) Putative side view (i.e., perpendicular to the membrane normal) of the *C*1 volume illustrating two distinct regions of pMMO-H termed the neck and base domains. (C) Sections ($x-y$ plane) through the pMMO-H complex as oriented in panel A with slices at 3.6 Å intervals taken from the base up to the neck (left to right). Black circles in panel C highlight examples of slices in which the organization of the protein domains forming a trimeric arrangement is clear. However, it can be seen that the organizations of these densities forming a triangular motif (circled) in both the base and neck regions are skewed with respect to each other.

only *C*2, *C*3, and *C*6 symmetries as possibilities. On the basis of this analysis, we also determined a 3D volume for a dimeric pMMO-H. The final volume with 2-fold rotational symmetry applied (data not shown) showed distinct differences in terms of gross structural features compared to the *C*1 structure and was visually very dissimilar. In addition, the central cleft clearly present in both membrane-bound pMMO and the *C*1 3D volume of purified pMMO-H was absent. Furthermore, the resolution of the reconstruction after applying *C*2 symmetry did not improve significantly at ~29 Å. The second approach involved calculation of a back projection of the *C*1 volume (orientated as in Figure 4A) projected along the putative axis of rotational symmetry. Rotational symmetry (SPIDER) by self-orientation analysis found peaks that corresponded to *C*2, *C*3, and *C*6 symmetries. However, upon separate examination of the neck and base domains, i.e., by slabbing away of the neck or base region, rotational symmetry analysis of the corresponding back projections found that the neck and base each exhibited a peak corresponding to only 3-fold (*C*3) rotational symmetry. Presented in Figure 4C are slices through the 3D volume as oriented in panel A (slice direction, from base to neck). Black circles on the Figure (panels 5 and 35) highlight slices in which the trimeric arrangement of protein domains is clear. However, it can be seen that the organization of these densities forming a triangular motif in both the base (panel 5) and neck (panel 35) regions are skewed with respect to each other. This may explain the observation of symmetry peaks corresponding to *C*6 but with the true symmetry actually being *C*3.

### *3D Structure of a Trimeric pMMO-H Complex*

In agreement with the biochemical data, and symmetry analysis of the 3D *C*1 pMMO-H volume, 3-fold rotational symmetry (*C*3) was applied in calculating a 3D structure of pMMO-H. Ten representative class averages displaying different orientations of pMMO-H are shown in panel I of Figure 5 (column a presenting class averages with corresponding back projections of the final *C*3 3D volume alongside in column b). The class averages show good agreement with the back projections of the *C*3 structure, demonstrating consistency with the final 3D volume. A vector plot of the distribution of particle orientations forming class averages used in the reconstruction showed good sampling of the 3D space required for projection matching (data not shown).

The 3D volume of the trimeric pMMO-H is displayed in panel II of Figure 5A−D using surface rendering (displayed 2$\sigma$ above the mean density calculated to encompass ~314 kDa). Presented in panel A is the putative "face-on" view (i.e., extending into the periplasm; see Discussion) characterized by three protein densities (labeled 1−3) surrounding a central canyon or cleft ~20−25 Å in diameter. The opposing face (panel B) is much flatter in comparison, sealed off from

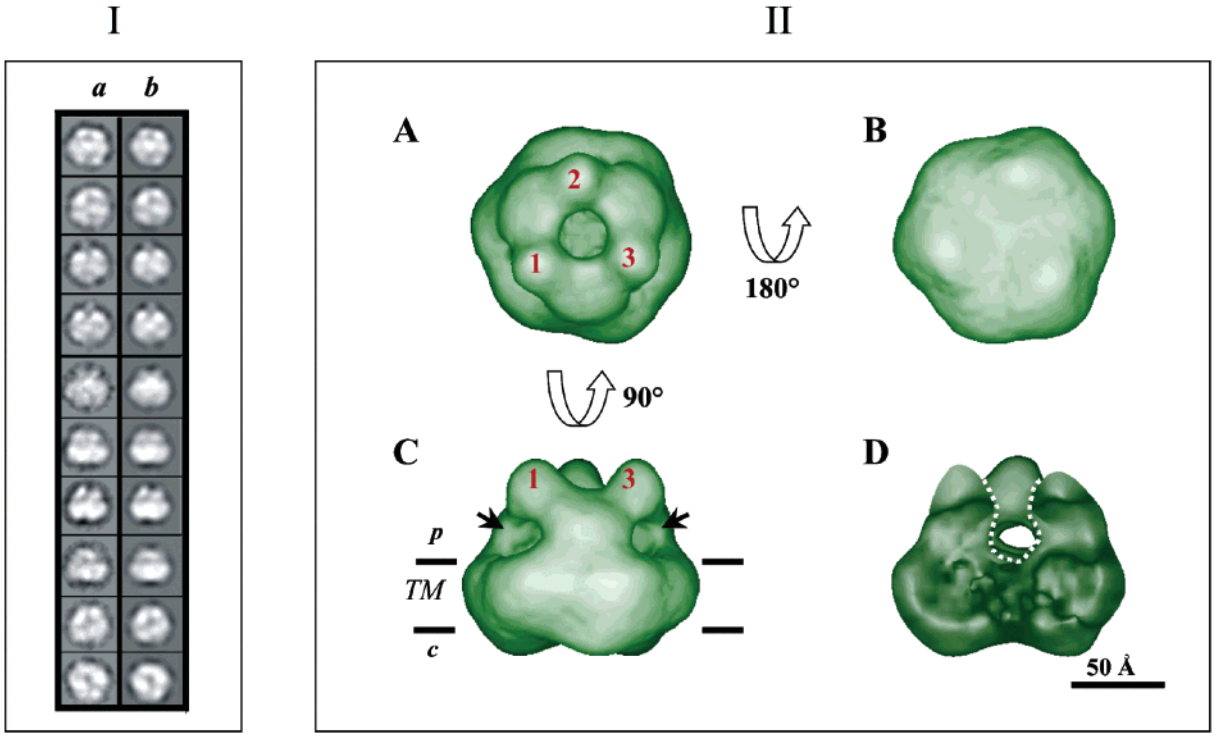


FIGURE 5: Image processing data and 3D structure of purified pMMO-H (*C*3 symmetry applied). In panel I, examples of class averages presenting different orientations of the pMMO-H complex used in the reconstruction are shown in column a. Comparison with the corresponding back projections of the final 3D volume (column b) finds good agreement and consistency between the class averages and the final 3D structure. Box size of 202 Å × 202 Å. In panel II is the surface-rendered 3D structure of pMMO-H at ~23 Å resolution (displayed 2$\sigma$ above the mean density) with *C*3 symmetry applied. (A) Putative periplasmic face of the complex characterized by three protein densities (labeled 1−3) surrounding a central cleft. (B) As viewed from the putative intracellular side showing a relatively flat complex approximately hexagonal in shape and ~135 Å across. (C) Rotation of the view in panel A by 90° presenting the putative side view. The black arrows indicate perforations holes in the outer surface. (D) Volume as oriented in panel C with the foremost half of the complex cut away to reveal the central cleft. TM denotes the transmembrane region, p the periplasm, and c the cytosol.

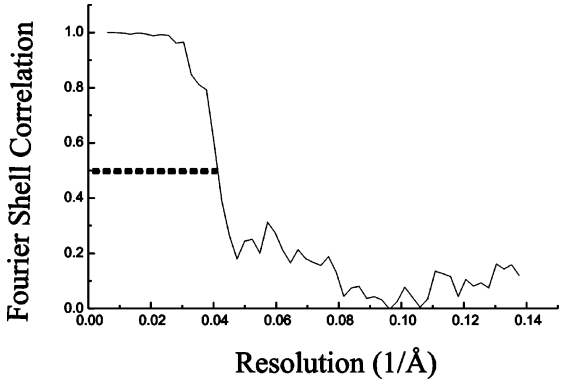


FIGURE 6: FSC plot showing the 3D (*C*3) reconstruction of purified pMMO-H at a resolution of ~ 23 Å.

the external milieu, and appears almost hexagonal in presentation, ~135 Å across. Rotation of the volume as oriented in panel A by 90° provides a putative side view as shown in panel C. In this orientation, the complex can be seen to have a height of ~110 Å, and as described for the *C*1 pMMO-H volume, the *C*3 structure is also resolved into two principal domains, the base and the neck. The complex narrows at the neck with a diameter of ~95 Å. Panel D shows the complex oriented as in panel C with the foremost half cut away to display the interior of the complex, revealing a canyon extending from the periplasmic side with a depth of ~55 Å and a diameter of 20−25 Å. The putative location of the lipid bilayer is indicated on in panel C. This assignment is based on topological analysis and by comparison with the recent crystal structure reported by Lieberman and Rosenzweig (*25*) (see Discussion and Figure 7 for comparison of the electron microscopy 3D volume and crystal structure, PDB entry 1YEW). Presented in Figure 6 is a Fourier shell correlation (FSC) plot indicating that the final 3D *C*3 volume is at a resolution of ~23 Å, the point at which the FSC is 0.5.

## DISCUSSION

*Oligomeric Form of pMMO-H.* The lack of the structural information of active pMMO impedes the understanding of its molecular mechanism. The information on the quaternary structure contributes significantly toward defining the molecular organization of the functional unit. To obtain this information, pMMO was solubilized using dodecyl maltoside and purified. The substrate assay indicated that the protein was stable and functional (Table 1). Although the specific activity of the purified pMMO-H is higher than that published recently (*16*, *24*, *47*), this activity is lower than that in membrane samples. It should be noted that in all published data, with only one exception, the activity of the purified pMMO is far lower than in the corresponding membrane preparations (see Table 1 in ref *47*). There are several well-established reasons for the loss of activity by integral proteins; most are due to changing the natural environment of the protein after solubilization and purification (*49*). Furthermore, the high specific activity of the hydroxylase in its membrane-embedded form is due to its close association with their natural electron-donating partners, type 2

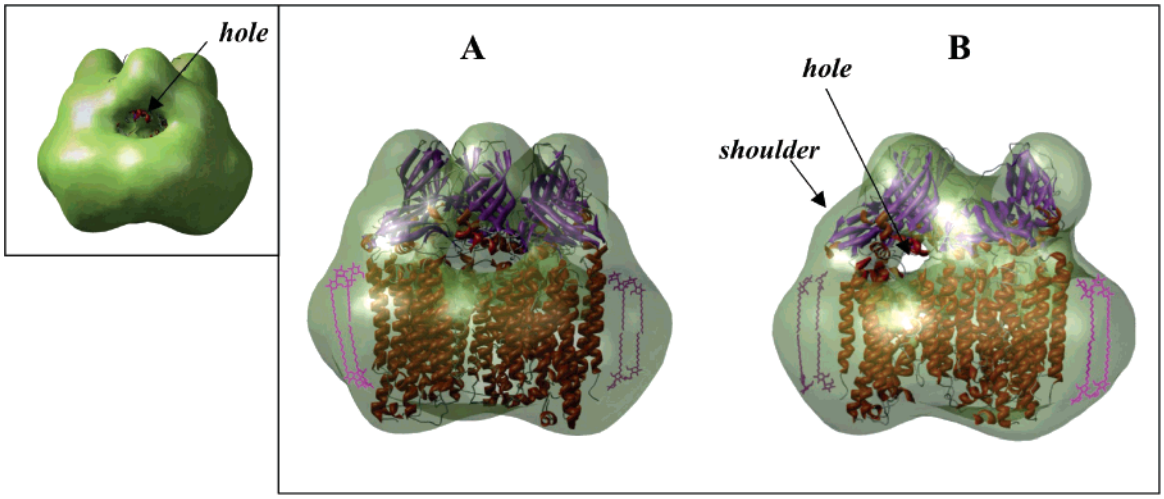


FIGURE 7: 3D EM structure (C3) of the purified, active, pMMO-H that accommodates the X-ray structure of pMMO-H described in ref *25*. (A) Putative side view of the 3D EM map (surface rendered in green with transparency factor set to 0.6, displayed 2$\sigma$ above the mean density) matched with the crystal structure, 1YEW (helices in red and $\beta$-sheets in purple) and four molecules of dodecyl $\beta$-D-maltoside (magenta, extracted from PDB entry 1qla). The inset shows the pMMO-H surface-rendered view, oriented as in panel A but with no transparency of the EM volume, illustrating that a region of low density (a hole) is present in both the EM and crystal structures, allowing access to a central cavity, a feature also common to both. (B) View in panel A rotated around the vertical axis ccw 60° illustrating a good match between the orientation of the neck domains and fitting of a shoulder domain with alignment of holes in both structures.

NADH dehydrogenase (*50*) and the elusive quinol. Removal of pMMO-H from membrane necessitates the use of an artificial electron donor, duroquinol, to drive the reaction. According to Shiemke and co-workers (*46*, *50*), duroquinol supported ~90% of the pMMO activity in solubilized samples compared with membrane-embedded samples. A decrease in pMMO activity after purification might be expected if one considers that duroquinol, which functions best in a lipid environment, has a low solubility in aqueous solution where it functions suboptimally. It is also possible that the other, as-yet-unknown, redox proteins may well be involved (*50*). Thus, in the absence of a full established electron transport chain for reduction of the pMMO in vivo, we believe that the close interaction between pMMO-H and its natural electron donor is tightly coupled and gives higher activities than the uncoupled, dissociated system such as purified membrane protein pMMO and artificial electron donor duroquinol.

According to SDS−PAGE of purified pMMO-H, the polypeptide bands have molecular masses corresponding to pMMO proteins at 47, 26, and 23 kDa. The doublet at 33/35 kDa is noticeably less intense in comparison. The principal difference noted between the polypeptide profiles before and after exposure of membrane-embedded pMMO to EDTA and NaCl was the significant reduction in intensity of a 21 kDa band and a band at ~63 kDa after washing, with the identity of the 21 kDa polypeptide unknown. However, these data clearly demonstrate that the polypeptides comprising pMMO are not removed by EDTA/salt washing and as such are likely to be embedded and/or anchored within the lipid bilayer. Our experiments have shown that washing with 10 mM EDTA inhibits ~50% of the specific activity of the partially purified pMMO (data not shown). However, washing has led to the removal of the extrinsic proteins with the advantage that the membrane-embedded pMMO-H complex has been exposed. This has permitted tentative analysis of the quaternary organization of pMMO-H in vivo (Figure 1). It should be noted that membranes employed for the solubilization and purification of pMMO-H, which were subsequently analyzed by electron microscopy and SPA, were not exposed to EDTA treatment and were active (see Table 1).

The amino acid sequence indicates that monomeric pMMO-H has a calculated molecular mass of 102.4 kDa, which agrees with that experimentally determined by SDS−PAGE, 96 kDa. The molecular mass of the purified pMMO oligomer described here is between 313 and 410 kDa, depending on the method used. It is known that the amount of detergent associated with purified intrinsic membrane proteins increases the mass of the protein, depending on the detergent, by a factor of 0.3−1.5 (*51*). The experiments with pMMO-H were carried out with dodecyl maltoside. Using the same detergent, the amount associated with mammalian cytochrome *c* oxidase was determined to be 35% of the molecular protein mass (*52*). Our data from BN-PAGE and gel filtration experiments have included some detergent. Assuming that the amount of detergent binding to the protein in our case is also ~35%, its real molecular mass should be around 300−310 kDa. This value is very close to the value of 313 ± 25 kDa calculated from equilibrium sedimentation result, which excluded detergent. From these data, we can confidently say that pMMO-H exists as a trimer in its oligomeric form. This conclusion is further reinforced by the application of two different methods of symmetry analysis of the structural data: one in which the symmetry of the individual raw particles was examined and the other using rotational symmetry analysis of back projections of the unsymmetrized *C*1 3D volume. Together, these data support the biochemical findings that the oligomeric form of the purified pMMO-H described here is trimeric.

This conclusion is distinct from the earlier results obtained by Lieberman et al. (*16*) and Yu et al. (*24*), which presented pMMO-H as a dimer and monomer, respectively, but is in agreement with the recent crystal structure described this year (*25*). The protocols used in the earlier work of Lieberman et al. and Yu et al. to purify pMMO-H did not include any protease inhibitors. We include benzamidine in our preparations to preserve the oligomeric nature of the enzyme.

Therefore, we suggest that the smaller oligomeric structures proposed (*16*, *24*) were due to nonspecific protein degradation. Also, the higher specific activities of our preparations confirmed that pMMO-H in our hands was less damaged during purification than those reported elsewhere.

The crystal structure of solubilized pMMO was published recently and thus gives us important information about a possible structural organization (*25*). However, activity assays were not attempted on the crystals, and as described previously, most purified samples from this laboratory were not active. Furthermore, no biochemical characterization of the oligomeric form was undertaken. These authors had previously indicated that pMMO was a dimer on the basis of molecular mass estimation by BN-PAGE (*16*, *47*); however, their newly presented structure of pMMO is a trimer. Trimeric forms of functional proteins are well-documented, e.g., ammonium transporter in the *E. coli* (*53*) and ion-selective receptors (*54*). A more pertinent example is light-harvesting complexes from *Marchantia polymorpha L*. (*55*) and multidrug resistance proteins (*56*).

We have now substantially advanced this field of research with the data presented here reporting a functionally active pMMO-H trimer, with data to tentatively suggest that this form is also found *in vivo*. Partially formed crystalline areas were observed in the ICMs isolated here, and though not well-ordered, refinement of the Fourier transform (after lattice unbending) found a trimeric organization as shown in Figure 1C. Though we cannot draw firm conclusions from the data extracted from the 2D crystals due to the lattice distortions, and the relatively small areas forming arrays, these results do lend further support to the concept of a trimeric organization of the pMMO-H complex in vivo.

*Comparison of the Crystal and EM Structure of a Trimeric pMMO-H.* Though the resolution of the 3D structure of pMMO-H presented in Figure 5 (panel II) does not allow confident delineation of the subunit boundaries, based on hydropathy plots, we suggest that each of the "arm: regions comprising the neck domain is formed by a pmoB (47 kDa) subunit. The view shown in Figure 5A (panel II) is likely to represent a face-on view of the complex since it is similar in terms of structural features to the membrane-embedded complexes shown in Figure 1A. On the basis of this interpretation, we propose that the complex is ~110 Å in height (i.e., as viewed perpendicular to the membrane normal). Working on the assumption that the bilayer is 40−50 Å thick, we have oriented the complex as shown in Figure 5C, which places the bulk of the protein within the bilayer, also in agreement with hydropathy studies, and matches the interpretation of the crystal structure (*25*) as shown in Figure 7.

It should be noted that negative staining techniques can lead to flattening of the structure, preferred orientations, or uneven staining. However, these effects and the extent or occurrence are very much sample-dependent. By comparison of the crystal structure (*25*) of pMMO-H and the medium-resolution 3D structure reported here, it is apparent that any artifacts of the negative staining preparation have not had any significant bearing. The recently published crystal structure, at 2.8 Å resolution, was shown to be cylindrical, with three monomers of pMMO-H forming a trimeric organization, ~105 Å in height and 90 Å in diameter. The soluble region was identified as extending and twisting up ~45 Å away from membrane. Presented in Figure 7 is the 3D structure of pMMO-H determined by electron microscopy and SPA matched with the crystal structure (PDB entry 1YEW) using Chimera (*57*). The height of the complex fits exactly into the 3D EM envelope with the three prominent domains (we labeled them 1−3, Figure 5A) forming the neck of the complex matching precisely the crystal structure in terms of both orientation and domain dimensions as shown in Figure 7A. Moreover, by rotation of the volume in panel A by 60° (counterclockwise around the vertical axis), a feature we have termed the "shoulder" is also matched in the crystal structure. The putative transmembrane domain (comprised of pmoA and pmoC) can be easily accommodated into the base domain. However, the base region of the EM volume was found to be wider with an approximately 20 Å belt of extra density surrounding the crystal trimer. Furthermore, the central cavity is sealed at the base in the EM volume, whereas in the crystal structure, it is continuous through the complex. One possible explanation that may account for both of these variations between the structures is the presence of detergent in the EM volume. The association of detergent with membrane proteins has been studied using neutron crystallography since due to the disordered character of the bulk detergent phase is not seen in crystal structures. Examples defining the detergent micelle include refs *58* and *59* in which the detergent was shown to form a belt around the membrane protein. The detergent was also found to occupy the central cavity formed by the nonameric arrangement of light-harvesting LH2 monomers (*58*) with the height of the central detergent cylinder being ~40 Å (detergent $\beta$-octyl glucoside). Therefore, the approximate dimensions and association of the detergent micelles previously described are consistent with the interpretation whereby a "life-belt" of detergent surrounds the pMMO-H transmembrane domain and forms a "plug" in the cavity from the base end. We extracted the coordinates of dodecyl $\beta$-D-maltoside (http://xray.bmc.uu.se/hicup/; PDB entry 1qla) and using Chimera (*57*) modeled four molecules of the detergent as shown in Figure 7 (DDM is magenta) for illustration and scale purposes. From these figures, it can be seem that it is conceivable that the extra density belt is formed by DDM micelles associating with the TM region of the complex. If this is indeed the case, then this has the advantage in that the region of the pMMO-H trimer residing within the lipid bilayer is delineated in the EM structure and can be correlated to the crystal structure. Some variations between the two structures (not withstanding differences in resolution) may also be expected since in this study single particles were examined as opposed to complexes locked into a defined conformation in a crystal lattice. Interestingly, the soluble domain identified in the crystal structure is skewed with respect to the transmembrane cylinder as also identified in the 3D EM volumes presented here. However, a further intriguing commonality between the crystal and EM structures is the identification of low-density regions within the neck domain. These "holes" in the soluble region of the pMMO-H trimer are not obviously apparent from inspection of the crystal structure; however, on comparison with the EM volume as shown in Figure 7, it can be seen that regions of low density can be matched in both structures.

A possible interpretation of the pMMO-H 3D volume is one whereby substrate entry into pMMO may involve entry

through the mouth or top of the canyon to reach the active site with products emitted through the holes at the neck and base intersection. This canyon was also identified in the crystal structure (*25*) as being 11 Å in a diameter at the top, widening to 22 Å where it extends into the membrane, although no role for this canyon in the structure was advanced. Another possible mode of action may be where the hydrophobic substrates diffuse into the upper leaflet of the membrane wherein they enter the pMMO-H complex through the side holes that lead into the central canyon; the hydrophilic products are then expelled through the aqueous filled canyon through the top of the structure into the extracellular medium. This second proposal would be similar to the "hydrophobic vacuum cleaner model" proposed for multidrug resistance transporters (*56*). However, as to whether the cavity is exposed to the exterior upon association of extrinsic polypeptides such as methanol dehydrogenase (MDH), the next enzyme in the methane pathway in methanotrophs, remains to be established.

In conclusion, we provide here data that present a model of a functional trimeric pMMO-H demonstrating an important link between structure and biological activity. Clearly, a priority for future work will be to explore pMMO at its different stages of purification to help understand the roles of extrinsic proteins such as methanol dehydrogenase.

## ACKNOWLEDGMENT

We thank Ms. Susan Slade for MS analysis and Dr. K. Jumel at NCMH, University of Nottingham, Nottingham, U.K., for help in the sedimentation equilibrium experiments. We also thank Dr. R. C. Ford, Dr. Al-Haji Bukar Kamis, Dr. M. Rosenberg, and Dr. S. M. Prince, University of Manchester, for useful discussion.

## REFERENCES

1. Wilshusen, J. H., Hettiaratchi, J. P. A., De Visscher, A., and Saint-Fort, R. (2004) Methane oxidation and formation of EPS in compost: Effect of oxygen concentration, *Environ. Pollut. 129*, 305−314.
2. Intergovernmental Panel on Climate Change (2001) in *Climate change 2001: The Scientific Basis*, Cambridge University Press, Cambridge, U.K.
3. Colby, J., Stirling, D. I., and Dalton, H. (1977) The soluble methane monooxygenase of *Methylococcus capsulatus* (Bath): Its ability to oxygenate *n*-akanes, *n*-alkenes, ethers, and acyclic, aromatic and heterocyclic compounds, *Biochem. J. 165*, 395−402.
4. Zatman, L. (1981) A search for patterns in methylotrophic pathway, in *Microbal Growth on $C_1$ Compounds* (Dalton, H., Ed.) pp 42−54, Heyden, London.
5. DiSpirito, A. A., Gulledge, J., Shiemke, A. K., Murell, J. C., Lidstrom, M. E., and Krema, C. I. (1992) Trichloroethylene oxidation by the membrane associated methane monooxygenase in type I, II and X methanotrophs, *Biodegradation 2*, 151−164.
6. Hanson, R. S., Netrusov, A. I., and Tsuji, K. (1991) The obligate methanotrophic bacteria *Methylococcus*, *Methylosinus*, *Methylomonas* and related bacteria, in *The Prokaryotes* (Balows, A., Truper, H. G., Dworkin, M., Harder, W., and Schleifer, K. H., Eds.) pp 2350−2365, Springer-Verlag, New York.
7. Fox, B. G., Borneman, J. G., Wackett, L. P., and Lipscomb, J. D. (1990) Haloalkene oxidation by the soluble methane monooxygenase from *Methylosinus trichosporium* OB3b: Mechanistic and environmental implications, *Biochemistry 29*, 6419−6427.
8. Prior, S. D., and Dalton, H. (1985) The effect of copper ions on membrane content and methane monooxygenase activity in methanol-grown cells *Methylococcus capsulatus* (Bath), *J. Gen. Microbiol. 131*, 155−163.
9. Rosenzweig, A. C., Frederick, C. A., Lippard, S. J., and Nordlund, P. (1993) Crystal-structure of a bacterial nonheme iron hydrohylase that catalyzes the biological oxidation of methane, *Nature 366*, 537−543.
10. Rosenzweig, A. C., Brandstetter, H., Whittington, D. A., Nordlund, P., Lippard, S. J., and Frederick, C. A. (1997) Crystal structures of the methane monooxygenase hydroxylase from *Methylococcus capsulatus* (Bath): Implications for substrate gating and component interactions, *Proteins 29*, 141−152.
11. Murrell, J. C., Gilbert, B., and McDonald, I. R. (2000) Molecular biology and regulation of methane monooxygenase, *Arch. Microbiol. 173*, 325−332.
12. Koh, S. C., Bowman, J. P., and Sayler, G. C. (1993) Soluble methane monooxygenase production and trichloroethylene degradation by type I methanotrophs *Methylomonos methanica* 68-1, *Appl. Environ. Microb. 59*, 960−967.
13. Smith, D. D. S., and Dalton, H. (1989) Solubilization of methane monooxygenase from *Methylococcus capsulatus* (Bath), *Eur. J. Biochem. 182*, 667−671.
14. Basu, P., Katterle, B., Andersson, K. K., and Dalton, H. (2003) The membrane-associated form of methane mono-oxygenase from *Methylococcus capsulatus* (Bath) is a copper/iron protein, *Biochem. J. 369*, 417−427.
15. Choi, D. W., Kunz, R. C., Boyd, E. C., Semrau, J. D., Antholine, W. E., Han, J. I., Zahn, J. A., Boyd, J. M., de la More, A. M., and DiSpirito, A. A. (2003) The membrane-associated methane monooxygenase (pMMO) and pMMO-NADH:quinone oxidoreductase complex from *Methylococcus capsulatus* Bath, *J. Bacteriol. 185*, 5755−5764.
16. Lieberman, R. L., Shrestha, D. B., Doan, P. E., Hoffman, B. M., Stemmler, T. L., and Rosenzweig, A. C. (2003) Purified particulate methane monooxygenase from *Methylococcus capsulatus* (Bath) is a dimer with both mononuclear copper and a copper-containing cluster, *Proc. Natl. Acad. Sci. U.S.A. 100*, 3820−3825.
17. Nguyen, H. H. T., Elliott, S. J., Yip, J. H. K., and Chan, S. I. (1998) The particulate methane monooxygenase from *Methylococcus capsulatus* (Bath) is a novel copper-containing three-subunit enzyme: Isolation and characterization, *J. Biol. Chem. 273*, 7957−7966.
18. Takeguchi, M., Miyakawa, K., and Okura, I. (1998) Purification and properties of particulate methane monooxygenase from *Methylosinus trichosporium* OB3b, *J. Mol. Catal. A: Chem. 132*, 145−153.
19. Miyaji, A., Kamachi, T., and Okura, I. (2002) Improvement of the purification method for retaining the activity of the particulate methane monooxygenase from *Methylosinus trichosporium* OB3b, *Biotechnol. Lett. 24*, 1883−1887.
20. Semrau, J. D., Chistoserdov, A., Lebron, J., Costello, A., Davagnino, J., Kenna, E., Holmes, A. J., Finch, R., Murrell, J. C., and Lidstrom, M. E. (1995) Particulate Methane Monooxygenase Genes in Methanotrophs, *J. Bacteriol. 177*, 3071−3079.
21. Zahn, J. A., Arciero, D. M., Hooper, A. B., and DiSpirito, A. A. (1996) Evidence for an iron center in the ammonia monooxygenase from *Nitrosomonas europaea*, *FEBS Lett. 397*, 35−38.
22. Prior, S. D., and Dalton, H. (1985) Acetylene as suicide substrate and active site probe for methane monooxygenase from *Methylococcus capsulatus* (Bath), *FEMS Microbiol. Lett. 29*, 105−109.
23. Tukhvatullin, I. A., Gvozdev, R. I., and Andersson, K. K. (2001) Structural and functional model of methane hydroxylase of membrane-bound monooxygenase from *Methylococcus capsulatus* (Bath), *Russ. Chem. Bull. 50*, 1867−1876.
24. Yu, S. S. F., Chen, K. H. C., Tseng, M. Y. H., Wang, Y. S., Tseng, C. F., Chen, Y. J., Huang, D. S., and Chan, S. I. (2003) Production of high-quality particulate methane monooxygenase in high yields from *Methylococcus capsulatus* (Bath) with a hollow-fiber membrane bioreactor, *J. Bacteriol. 185*, 5915−5924.
25. Lieberman, R. L., and Rosenzweig, A. C. (2005) Crystal structure of a membrane-bound metalloenzyme that catalyses the biological oxidation of methane, *Nature 434*, 177−182.
26. Sato, C., Ueno, Y., Asai, K., Takahashi, K., Sato, M., Engel, A., and Fujiyoshi, Y. (2001) The voltage-sensitive sodium channel is a bell-shaped molecule with several cavities, *Nature 409*, 1047−1051.
27. Sokolova, O., Kolmakova-Partensky, L., and Grigorieff, N. (2001) Three-dimensional structure of a voltage-gated potassium channel at 2.5 nm resolution, *Structure 9*, 215−220.
28. Wang, M. C., Collins, R. F., Ford, R. C., Berrow, N. S., Dolphin, A. C., and Kitmitto, A. (2004) The three-dimensional structure of the cardiac L-type voltage-gated calcium channel: Comparison

with the skeletal muscle form reveals a common architectural motif, *J. Biol. Chem. 279*, 7159−7168.
29. Rosenberg, M. F., Callaghan, R., Ford, R. C., and Higgins, C. F. (1997) Structure of the multidrug resistance P-glycoprotein to 2.5 nm resolution determined by electron microscopy and image analysis, *J. Biol. Chem. 272*, 10685−10694.
30. Okorokov, A. L., Orlova, E. V., Kingsbury, S. R., Bagneris, C., Gohlke, U., Williams, G. H., and Stoeber, K. (2004) Molecular structure of human geminin, *Nat. Struct. Mol. Biol. 11*, 1021−1022.
31. Ruprecht, J., and Nield, J. (2001) Determining the structure of biological macromolecules by transmission electron microscopy, single particle analysis and 3D reconstruction, *Prog. Biophys. Mol. Biol. 75*, 121−164.
32. Whittenbury, R., Phillips, K. C., and Wilkinson, J. F. (1970) Enrichment, isolation and some properties of methane utilising bacteria, *J. Gen. Microbiol. 61*, 205−218.
33. Lowry, O. H., Rosenbrough, N. G., Farr, A. L., and Randall, R. J. (1951) Protein measurement with the Folin fenol reagent, *J. Biol. Chem 193*, 265−275.
34. Schagger, H. (2003) Blue native gel electrophoresis, in *Membrane protein purification and crystallisation* (Hunte, C., Von Jagov, G., and Schagger, H., Eds.) pp 105−130, Academic Press, London.
35. Schagger, H., and Von Jagov, G. (1991) Blue native electrophoresis for isolation of membrane protein complexes in enzymatically active form, *Anal. Biochem. 199*, 223−231.
36. Laemmli, U. K. (1970) Cleavage of the structural proteins during the assembly of the head of the bacteriophage T4, *Nature 227*, 680−685.
37. Kleinekofort, W., Germeroth, L., van de Brock, J. A., Schubert, D., and Michel, H. (1992) The light-harvesting complex II(B800/850) from *Rhodospirillium molischianum* is an octamer, *Eur. J. Biochem. 1140*, 102−104.
38. Hoppert, M., and Holzenburg, A. (1998) Preparation techniques for transmission electron microscopy (TEM), in *Electron Microscopy in Microbiology: RMS Handbook Series* (Hoppert, M., and Holzenburg, A., Eds.) pp 11−18, BIOS Scientific Publishers Ltd., Oxford, U.K.
39. Hovmoller, S. (1992) Crisp: Crystallographic Image-Processing on a Personal-Computer, *Ultramicroscopy 41*, 121−135.
40. Crowther, R. A., Henderson, R., and Smith, J. M. (1996) MRC image processing programs, *J. Struct. Biol. 116*, 9−16.
41. Ludtke, S. J., Baldwin, P. R., and Chiu, W. (1999) EMAN: Semiautomated software for high-resolution single-particle reconstructions, *J. Struct. Biol. 128*, 82−97.
42. Bottcher, B., Wynne, S. A., and Crowther, R. A. (1997) Determination of the fold of the core protein of hepatitis B virus ky electron cryomicroscopy, *Nature 386*, 88−91.
43. Harauz, G., and Vanheel, M. (1986) Exact Filters for General Geometry 3-Dimensional Reconstruction, *Optik 73*, 146−156.
44. Frank, J., Radermacher, M., Penczek, P., Zhu, J., Li, Y. H., Ladjadj, M., and Leith, A. (1996) SPIDER and WEB: Processing and visualization of images in 3D electron microscopy and related fields, *J. Struct. Biol. 116*, 190−199.
45. Zahn, J. A., Bergmann, D. J., Boyd, J. M., Kunz, R. C., and DiSpirito, A. A. (2001) Membrane-associated quinoprotein formaldehyde dehydrogenase from *Methylococcus capsulatus* Bath, *J. Bacteriol. 183*, 6832−6840.
46. Shiemke, A. K., Cook, S. A., Miley, T., and Singleton, P. (1995) Detergent solubilization of membrane-bound methane monooxygenase requires plastoquinol analogs as electron donors, *Arch. Biochem. Biophys. 321*, 421−428.
47. Lieberman, R. L., and Rosenzweig, A. C. (2004) Biological methane oxidation: Regulation, biochemistry, and active site structure of particulate methane monooxygenase, *Crit. Rev. Biochem. Mol. Biol. 39*, 147−164.
48. le Maire, M., Champeil, P., and Moller, J. V. (2000) Interaction of membrane proteins and lipids with solubilizing detergents, *Biochim. Biophys. Acta 1508*, 86−111.
49. Arora, A., and Tamm, L. K. (2001) Biophysical approaches to membrane protein structure determination, *Curr. Opin. Struct. Biol. 11*, 540−547.
50. Cook, S. A., and Shiemke, A. K. (2002) Evidence that a type-2 NADH:quinone oxidoreductase mediates electron transfer to particulate methane monooxygenase in *Methylococcus capsulatus*, *Arch. Biochem. Biophys. 398*, 32−40.
51. Gennis, R. B. (1989) Biomembranes, Molecular Structure and Function, in *Biomembranes, Molecular Structure and Function* (Cantor, C. R., Ed.) pp 91−105, Springer-Verlag, New York.
52. Suarez, M. D., Revzin, A., Narlock, R., Kempner, E. S., Thompson, D. A., and Fergusonmiller, S. (1984) The Functional and Physical Form of Mammalian Cytochrome-C Oxidase Determined by Gel-Filtration, Radiation Inactivation, and Sedimentation Equilibrium-Analysis, *J. Biol. Chem. 259*, 3791−3799.
53. Blakey, D., Leech, A., Thomas, G. H., Coutts, G., Findlay, K., and Merrick, M. (2002) Purification of the *Escherichia coli* ammonium transporter AmtB reveals a trimeric stoichiometry, *Biochem. J. 364*, 527−535.
54. Nicke, A., Baumert, H. C., Rettinger, J., Eichele, A., Lambrecht, G., Mutschler, E., and Schmalzing, G. (1998) $P2X_1$ and $P2X_3$ receptors form stable trimers: A novel structural motif of ligand-gated ion channels, *EMBO J. 17*, 3016−3028.
55. Harrer, R. (2003) Associations between light-harvesting complexes and Photosystem II from *Marchantia polymorpha L*. determined by two- and three-dimensional electron microscopy, *Photosynth. Res. 75*, 249−258.
56. Murakami, S., Nakashima, R., Yamashita, E., and Yamaguchi, A. (2002) Crystal structure of bacterial multidrug efflux transporter AcrB, *Nature 419*, 587−593.
57. Pettersen, E. F., Goddard, T. D., Huang, C. C., Couch, G. S., Greenblatt, D. M., Meng, E. C., and Ferrin, T. E. (2004) UCSF chimera: A visualization system for exploratory research and analysis, *J. Comput. Chem. 25*, 1605−1612.
58. Prince, S. M., Howard, T. D., Myles, D. A. A., Wilkinson, C., Papiz, M. Z., Freer, A. A., Cogdell, R. J., and Isaacs, N. W. (2003) Detergent structure in crystals of the integral membrane light-harvesting complex LH2 from *Rhodopseudomonas acidophila* strain 10050, *J. Mol. Biol. 326*, 307−315.
59. Roth, M., Lewitbentley, A., Michel, H., Deisenhofer, J., Huber, R., and Oesterhelt, D. (1989) Detergent Structure in Crystals of a Bacterial Photosynthetic Reaction Center, *Nature 340*, 659−662.

BI050820U